Hindawi
Geofluids
Volume 2020, Article ID 8863898, 14 pages
https://doi.org/10.1155/2020/8863898

Research Article

Experimental Study on the Self-Healing Behavior of Fractured Rocks Induced by Water-CO_2-Rock Interactions in the Shendong Coalfield

Jinfeng Ju,[1,2] Quansheng Li,[3] and Jialin Xu[4,5]

[1]*The National and Local Joint Engineering Laboratory of Internet Application Technology on Mine, China University of Mining and Technology, Xuzhou 221008, China*
[2]*IoT/Perception Mine Research Center, China University of Mining and Technology, Xuzhou, Jiangsu 221008, China*
[3]*State Key Laboratory of Water Resources Protection and Utilization in Coal Mining, Beijing 100011, China*
[4]*State Key Laboratory of Coal Resources and Safe Mining, Xuzhou, Jiangsu 221116, China*
[5]*School of Mines, China University of Mining and Technology, Xuzhou, Jiangsu 221116, China*

Correspondence should be addressed to Jialin Xu; xujlcumt@163.com

Received 7 July 2020; Revised 3 September 2020; Accepted 15 September 2020; Published 8 October 2020

Academic Editor: Keni Zhang

Copyright © 2020 Jinfeng Ju et al. This is an open access article distributed under the Creative Commons Attribution License, which permits unrestricted use, distribution, and reproduction in any medium, provided the original work is properly cited.

This study experimentally investigated the self-healing behavior, referring to the naturally occurring water permeability decrease, of fractured rocks exposed to water-CO_2-rock interaction (WCRI). The experiment was conducted on prefractured specimens of three rock types typical of the Shendong coalfield: coarse-grained sandrock, fine-grained sandrock, and sandy mudrock. During the experiment, which ran for nearly 15 months, all three specimens exhibited decreasing permeabilities. The coarse- and fine-grained sandrock specimens exhibited smooth decreases in permeability, with approximately parallel permeability time curves, whereas that of the sandy mudrock specimen decreased rapidly during the initial stage and slowly during later stages. The sandrock specimens were rich in feldspars, which were dissolved and/or corroded and involved in ionic exchange reactions with CO_2 and groundwater, thereby generating secondary minerals (such as kaolinite, quartz, and sericite) or $CaSO_4$ sediments. These derivative matters adhered to the fracture surface, thereby gradually repairing fractures and decreasing the water permeability of the fractured rocks. In comparison, the sandy mudrock had a high content of clay minerals, and the water-rock interaction caused rapid expansions of illite, mixed illite-smectite, and other clay minerals, thereby narrowing the fractures and causing the rapid permeability decrease during the initial stage. In later stages, the derivative matters generated by the dissolution and/or corrosion of feldspars and other aluminum silicate minerals in the mudrock filled and sealed the fractures, causing the slow permeability decreases during the later stages, as in the sandrock specimens. Neutral and basic groundwater conditions facilitated better self-healing of fractured mudrocks rich in clay minerals, whereas acidic groundwater conditions and the presence of CO_2 facilitated better self-healing of fractured sandrocks. Thus, this study's results are of significant value to aquifer restoration efforts in the Shendong coalfield and other ecologically vulnerable mining areas.

1. Introduction

The Shendong coalfield is located in the Maowusu Desert, West China, which has an arid or semiarid climate, vulnerable ecology and environment, and scarce water resources. With increasing coal mining in recent years, there is a growing tension between environmental protection and high-efficiency coal mining in this area. Therefore, the need to implement water-conserving mining technologies has become increasingly urgent [1].

Aquifers have conventionally been conserved by controlling the height of water-conducting fracture development [2–6]. However, this approach limits mining output and efficiency and is therefore not suitable for the Shendong

coalfield. Instead, postmining storage and utilization of the groundwater lost during mining and the ecological restoration of damaged aquifers are strategies that are considered more suitable for this coalfield [2]. After many years of research and practice, Gu [7] developed an underground reservoir technology for water preservation, in which the underground goaf is engineered to store and purify groundwater lost during coal mining for subsequent use. The technology has been applied in 15 mines in the Shendong coalfield and has effectively alleviated water consumption issues in this mining area [7–10]. This technology transfers and stores water by draining groundwater accessed in the mining process to a stope for conservation. Thus, this technology alters the original groundwater network and, if water-conducting fractures are connected with loose surface layers, may even induce the release of near-surface water. In this situation, manual irrigation is usually necessary to satisfy the water requirements of ground vegetation, and ecological restoration of mining-damaged aquifers is therefore another water-conservation approach that is urgently needed for such mining areas.

The root cause of mining-induced groundwater loss lies in water-conducting fractures, and limiting the water-conduction capacity of fractures is key to restoring mining-damaged aquifer ecology [1, 2]. Grouting is presently the simplest and most effective technology for sealing water-conducting fractures [11–13]. However, grout injections cannot effectively seal these fractures in the presence of strong hydrodynamic erosion, or when the fractures are sufficiently extensive that they cannot adequately enclose the grout without undue expense.

Field engineering practice has shown that water-conducting fractures can exhibit some degree of self-healing. After a long period of evolution, the water-conduction capacity of the fractures decreases, and the area of the water-conducting fractured zone diminishes, thereby reducing groundwater loss and increasing groundwater levels. For example [1], in the initial mining stage of Panel IV (1-2 coal), at Bulianta Mine in Shendong coalfield, water-conducting fractures spread to the bedrock-roof interface, and the water originally observed in surface hydrological drill holes was completely lost. However, as the working face continued to advance, the water level in the drill holes gradually recovered. Gu and Zhang [14] applied a high-precision four-dimensional multiattribute seismic prospecting method to identify variations in the groundwater environment of a fully-mechanized working face in the Shendong coalfield. They compared the overlying water content distributions before and after coal seam mining and found that the rocks in the fractured zone could recover their initial structures under mining-induced stress, thereby gradually reducing groundwater loss.

An understanding of the mechanism and effects of this self-healing behavior would significantly advance the development of techniques that limit the water flow through mining-fractured rocks and restore the aquifer ecosystem. Studies [15–22] have shown that the self-healing of water-conducting fractures is enabled by mining-induced stress and physiochemical interactions among the groundwater, stope air, and fractured rock. The major mechanisms underlying the self-healing behavior include the hydrophilic expansion of clay minerals to narrow the fracture space, the filling and sealing of the fracture space by chemical sediments and secondary minerals resulting from the ionic exchange at the water-air-rock interface, and the compaction of water-immersed and softened rocks under the effect of mining-induced stress. Thus, the mechanisms underlying the self-healing behavior of water-conducting fractures and the final remedial effect are closely related to the physiochemical characteristics of water, air, and rock; the distribution of mining-induced stress; and the cumulative self-healing time. Therefore, the influence of each of the relevant factors on the self-healing behavior of water-conducting fractures must be investigated.

In the present study, the interaction at the water-air-rock interface was experimentally investigated with the aim of elucidating the various self-healing behaviors of fractures with different lithological properties. The experimental environment consisted of specimens prepared from three rocks typical of the Shendong coalfield (coarse-grained sandrock, fine-grained sandrock, and sandy mudrock), CO_2 (as the major component of stope air), and a neutral water solution that simulated groundwater.

2. Experimental Methods

2.1. Rock Sampling and Specimen Preparation. Samples of the following three rock types, all typical of the Shendong coalfield, were collected: coarse-grained sandrock, fine-grained sandrock, and sandy mudrock. The mineral compositions of the three types were analyzed using X-ray diffraction (XRD), with the results presented in Table 1. The rocks mainly consisted of quartz, potassium feldspar, plagioclases (mainly albite, andesine, and anorthite), and clay minerals (mainly kaolinite). A standard cylindrical specimen (measuring 5 cm in diameter and 10 cm in height) was prepared from each of the rock types. To simulate mining-induced fractures, the rock specimens are artificially destroyed using an MTS compression testing machine (MTS Systems Corp.) through uniaxial loading, as depicted in Figure 1.

2.2. Simulation of Groundwater. The groundwater in the Shendong coalfield is generally neutral or weakly basic [23] and was therefore simulated using a neutral water solution (pH = 6.24), which was prepared using a Na_2SO_4 reagent and deionized water. Table 2 presents the ionic compositions of the water solution before and after the experiment.

2.3. Experimental Procedure. Each fractured rock specimen was placed in a sealed container to simulate the water-CO_2-rock interaction (WCRI), as shown in Figure 2. Prior to placement in the container, the cylindrical sides of the specimen were evenly coated with silicone rubber to prevent interactions between the fractures and the external environment, and an isolation ring was adhered 1–2 cm from the bottom of the specimen. The specimen-ring assembly was then placed in the container, with the ring adhered to the container wall, and the gap between the specimen and container wall sealed with resin. After the resin had completely solidified, the container was filled with the simulated

Table 1: Mineral compositions of specimen surfaces before and after the experiment (%).

Rock samples Rock character	Experimental stage	Quartz	Potassium feldspar	Plagioclase	Clay minerals					
					Total content	I/S	It	K	C	S%
Coarse-grained sandrock	BE	47	26	24	3	—	2	96	2	—
	AE	50	23	24	3	—	2	97	1	50
Fine-grained sandrock	BE	54	14	24	8	6	12	73	9	10
	AE	57	12	23	8	6	10	78	6	57
Sandy mudrock	BE	39	17	30	14	51	21	16	12	20
	AE	44	14	31	11	50	20	20	10	16

Notes: the table lists the relative proportions of the minerals to the total detected content rather than the overall content since some minerals are undetectable. K means kaolinite, C means chlorite, It means illite, and I/S means mixed illite-smectite layers minerals, and S% is the illite proportion in layers of mixed illite and smectite; BE means before the experiment, and AE means after the experiment.

Figure 1: Fractured rock specimens (from left to right: coarse-grained sandrock, fine-grained sandrock, and sandy mudrock).

groundwater solution, such that the water solution could only flow from the top to the bottom of the specimen through its fractures. CO_2 was supplied into the container through a pipe, at a flow rate controlled to 4–6 mL/min [22], simulating the CO_2 concentration in typical stopes, and was monitored using a microgas-flow sensor. The working seams in the Shendong coalfield are shallow, and the temperature of the environment surrounding the underground rock masses in this mining area is essentially similar to normal atmospheric temperature. Thus, the ambient temperature was set to normal atmospheric temperature in the experiment.

During the course of the experiment, the absolute permeability of the specimen was tested at 1- to 2-week intervals. Considering that the permeability of fractured rock specimens is significantly greater than that of intact rock specimens, the permeability test on fractured rock specimens can be realized by means of self-weight and seepage. Hence, the aqueous solution was not pressurized by any devices. In these tests, the drain valve was opened to test the fluid flow, and two methods were carried out to ensure the measurement accuracy. Method 1: directly determine the time taken for the liquid level of the aqueous solution above the rock specimen to drop a certain height (for example, 1 cm; the external surface of the container was equipped with a graduated scale). Thereafter, calculate the seepage discharge over the corresponding period of time, according to the inner diameter of the container and the reduced height of the liquid level. Method 2: after the aqueous solution at the lower part of the rock specimens flowed out (and stored in a beaker or other containers), measure the amount of aqueous solution flowing out from the drain valve over a certain fixed period of time (such as 1 min) using a small-range measuring cylinder; the values obtained by these two methods can be corrected mutually. In practice, more than three fluid flow tests were performed, and the values were averaged. The temperature of the water solution was measured to determine the solution's viscosity, and then, the water permeability value K could finally be determined according to Eq. (1), where Q is the water flow per unit time, A is the inner cross-sectional area of the container, μ is the solution's viscosity, L is the height of the rock specimen, and ΔP is the pressure difference before and after water flow through the rock specimen. After each measurement, the discharged water solution was poured back into the WCRI container. The experiment was run continuously for nearly 15 months, after which period the specimen was taken out of the container, and the water solution was discharged from the container.

$$K = \frac{Q\mu L}{\Delta P A} \tag{1}$$

2.4. Mineral Composition and Water Chemistry Analysis. To analyze the influence of long-duration WCRI on the variations in mineral composition at the fracture surface, the rock samples were collected and tested before and after the experiment. Prior to the experiment, the testing samples were collected from the scrap material cut when processing the rock specimens. As the experiments finished and the rock specimens taken out of the container, the specimens were taken apart along the fracture surface; thereafter, the cutting tool is used to break down the rock near the fracture surface. Then, grinding and testing was performed. The microstructures and morphologies of minerals at the fracture surfaces of the three prefractured rock specimens were analyzed using scanning electron microscopy (SEM), and the contents of the fracture-surface minerals were examined via XRD. Accordingly, the ionic composition of the water solution was also tested. Finally, the measurements from before and after the experiment were then compared to investigate the relationship between the water permeability of the specimens and the variation in the chemical compositions of both the water solution and the specimens.

Table 2: Contents (mg/L) of major ions and pH values of the water solution before and after the experiment.

Experimental stage		Na^+	SO_4^{2-}	HCO_3^-	Cl^-	NH^{4+}	K^+	Ca^{2+}	Mg^{2+}	PH
Before the experiment	Original solution	769.4	1434.8	10.3	5.6	—	0.1	0.1	—	6.24
After the experiment	Experiment with coarse-grained sandrock	1007.4	2543.7	443.55	37.2	16.7	13.1	329.3	40.2	7.42
	Experiment with fine-grained sandrock	1071.5	2129.6	626.1	86.9	8.6	12.6	172.7	35.3	7.68
	Experiment with sandy mudrock	858.4	1367.7	817.8	34.6	2.5	11.8	119.7	232.6	7.33

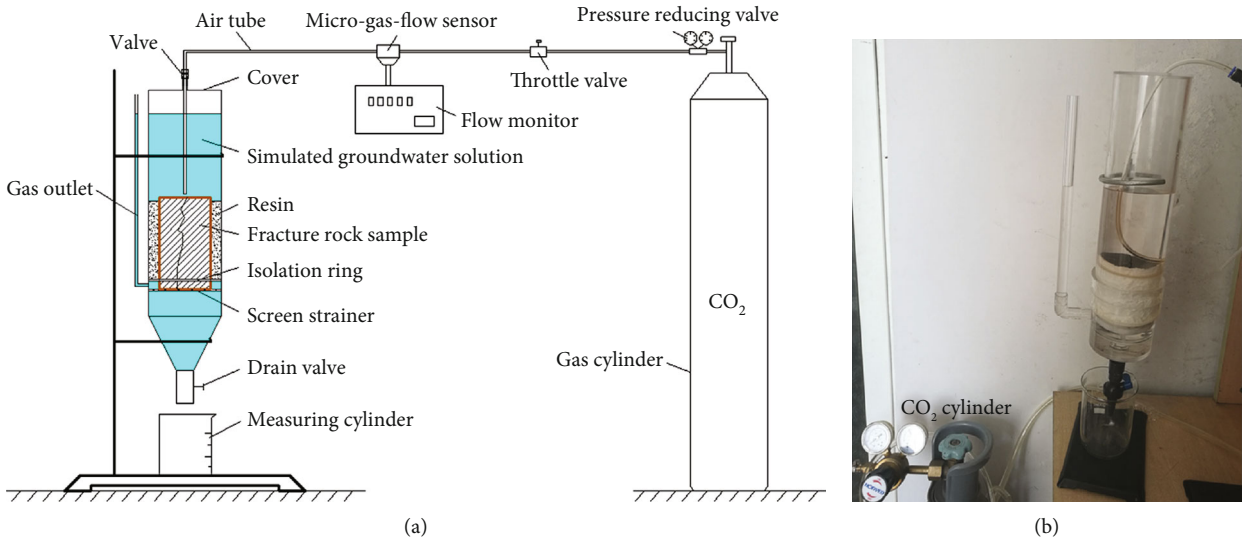

Figure 2: Set-up for the water-CO_2-rock interaction (WCRI) experiment. (a) Illustration. (b) Photo.

3. Results and Discussion

3.1. Variations in the Water Permeability. The nearly 15-month WCRI experiment generated water permeability data that showed patterns of variation in the three prefractured rock specimens. Figure 3 shows the remarkable decreases in the absolute permeability over time of all three specimens. The permeability curves of the coarse-grained sandrock specimen and the fine-grained sandrock specimen were similar: the permeability of the former decreased from 3.27×10^{-11} m^2 at the beginning of the experiment to 1.26×10^{-11} m^2 at the end, with an average decrease of 4.5×10^{-14} m^2/day, whereas that of the latter decreased from 2.40×10^{-11} m^2 to 6.65×10^{-12} m^2, with a slightly lower average decrease of 3.9×10^{-14} m^2/day. In contrast, the permeability of the sandy mudrock specimen decreased in stages. This specimen's absolute permeability decreased rapidly from 8.48×10^{-11} m^2 to 2.93×10^{-11} m^2 during the initial 80-day period, with an average decrease of 6.94×10^{-13} m^2/day, and then decreased slowly to 9.6×10^{-12} m^2 during the subsequent 321-day period, with an average decrease of 6×10^{-14} m^2/day. In both stages, the permeability of the sandy mudrock decreased at significantly higher rates than those of the coarse- and fine-grained sandrocks. This difference was closely related to the different mineral compositions of the three specimens, as further discussed in Section 3.4.

A similar WCRI experiment can be found in Ref. [22] on a prefractured sandy mudrock specimen and simulated the groundwater using both acidic and basic water solutions. The water permeability curves yielded by that experiment exhibited a similarly staged decreasing pattern, as shown in Figure 4. Combining Figures 3 and 4, the staged permeability decrease can be seen to be more pronounced when the groundwater was simulated using a basic or neutral water solution rather than the acidic solution. Furthermore, considering the results in Ref. [22] in conjunction with those of the present study, this staged permeability decrease can be attributed to the sandy mudrock's content of minerals that accommodate high degrees of hydrophilic expansion. Comparing Figures 3 and 3, the permeability of the mudrock at the end of the present experiment was much higher (by an order of magnitude), and the magnitude of the permeability decrease (defined as the ratio of absolute permeability at the beginning of experiment to that at the end of experiment) was significantly smaller, despite the longer duration of the present experiment (almost twice long). These results may be explained by the different specimen pretreatments (type and size of fracturing) or initial permeabilities established in the two experiments: more developed and larger fractures would be expected to result in higher initial permeabilities and smaller WCRI-induced self-healing effects, such that larger fractures would be more difficult to seal through self-healing.

3.2. Variations in Mineral Composition at the Fracture Surface

3.2.1. Variations in the Microstructures of Mineral Crystals at the Fracture-Surface. During the nearly 15-month WCRI

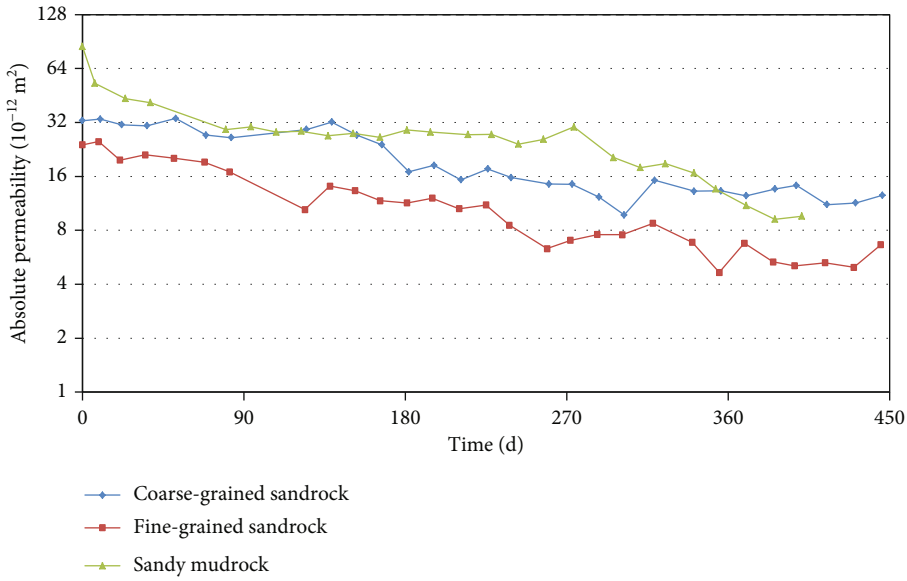

Figure 3: Absolute permeability of the three specimens over time.

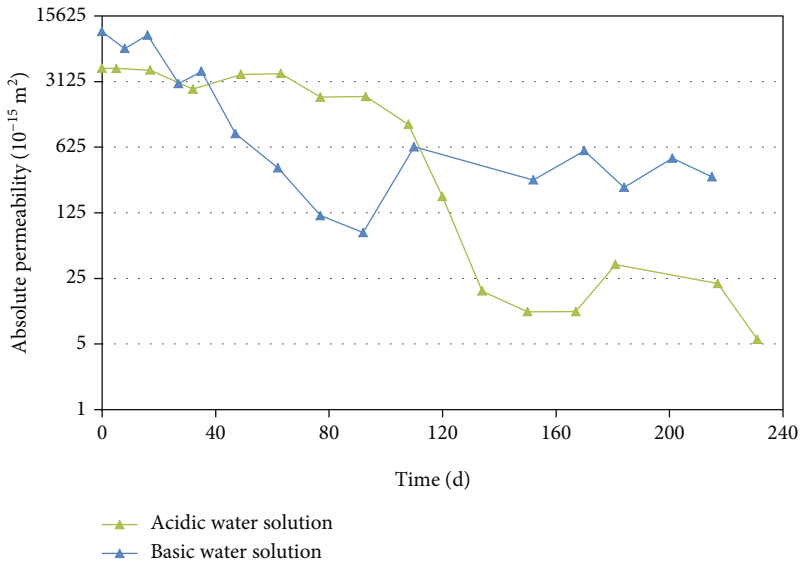

Figure 4: Absolute permeability over time of a previously reported prefractured sandy mudrock specimen [22].

experiment, all of the specimens exhibited significant changes in these characteristics, including phenomena, such as the dissolution and/or corrosion of primary minerals and the generation of secondary minerals.

Figure 5 depicts the microstructures and morphologies of minerals at the fracture surface of the coarse-grained sandrock before and after the experiment. The feldspars (potassium feldspar and plagioclases), which constituted a big proportion of the rocks, showed particularly significant dissolution and/or corrosion. For example, before the experiment, potassium feldspar crystals (marked by rectangles in the SEM images and identified from the O, K, Si, and Al found via energy dispersion spectrum (EDS) analysis) exhibited regular prism shapes, with smooth surfaces and sharp edges and angles (Figure 5(a)), whereas they exhibited clear corrosion-induced holes at the surface after the experiment (Figure 5(b)). Albite crystals exhibited similar changes (Figures 5(c) and 5(d)), with the crystal surfaces markedly coarsened and fragmented after the experiment. In contrast, clay minerals, which constituted a small proportion of the rocks, did not undergo significant dissolution and/or corrosion.

In addition, secondary minerals were observed to adhere to the primary minerals at the fracture surface, as shown in Figure 6. On the surfaces of regular-polyhedron-shaped quartz crystals were many fragmented, flake-shaped minerals; EDS analysis showed that these secondary crystals consisted of three elements (O, Si, and Al), and the crystals were thus identified as kaolinite. The microstructure and morphology of the secondary kaolinite were different from

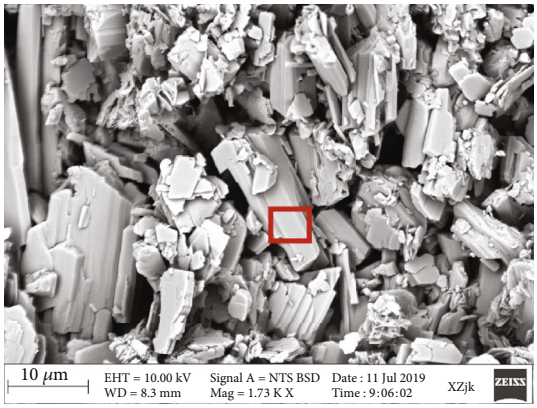

Element	Wt%	At%
O K	53.62	67.52
Al K	8.69	6.49
Si K	27.54	19.75
K K	9.67	6.07
Fe K	0.48	0.17

(a)

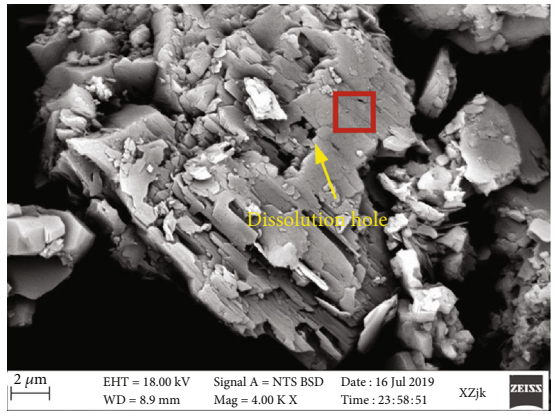

Element	Wt%	At%
O K	55.67	67.91
Al K	8.55	6.19
Si K	27.23	18.92
K K	8.00	6.79
Fe K	0.55	0.19

(b)

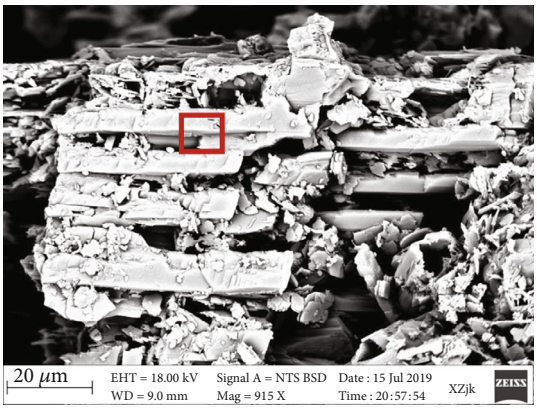

Element	Wt%	At%
O K	35.93	48.79
Na K	7.44	7.04
Al K	11.91	9.58
Si K	44.73	34.59

(c)

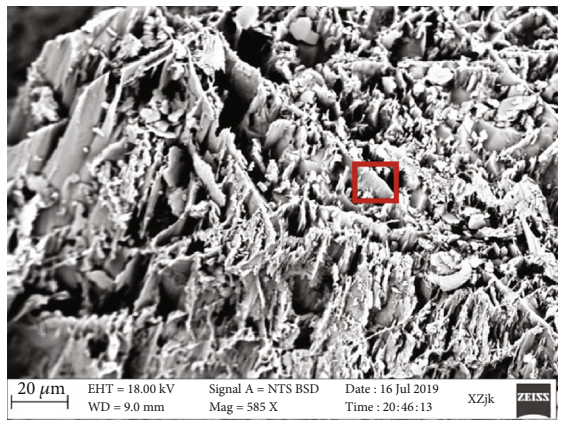

Element	Wt%	At%
O K	56.31	68.61
Na K	6.84	5.80
Al K	9.03	6.53
Si K	26.62	18.48
Ca K	1.22	0.59

(d)

Figure 5: Micromorphologies of feldspar crystals at the fracture surface in the coarse-grained sandrock specimen before and after the experiment. (a) Potassium feldspar crystals (before the experiment). (b) Corroded potassium feldspar crystals (after the experiment). (c) Albite crystals (before the experiment). (d) Corroded albite crystals (after the experiment). Note: to confirm the mineral composition in the areas marked by the rectangles, an energy dispersion spectrum (EDS) analysis was performed, and the results are presented in the tables below the SEM images (the same below). In the tables, Wt% means weight percentage, At% means Atomic percentage, and the same below.

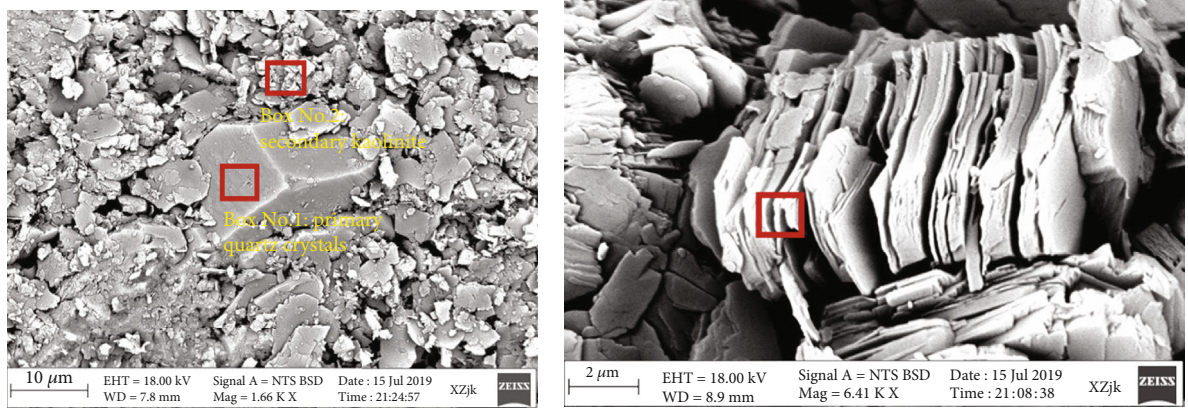

(a) (b)

Element	Wt%	At%
O K	29.87	42.78
Si K	70.13	57.22

(c)

Element	Wt%	At%
O K	47.46	61.08
Al K	13.65	10.43
Si K	38.88	28.51

(d)

Element	Wt%	At%
O K	48.40	61.78
Al K	23.70	17.94
Si K	27.89	20.28

(e)

Figure 6: Secondary minerals adhering to the primary minerals at the fracture surface in the coarse-grained sandrock specimen. (a) Secondary kaolinite adhering to the quartz crystals after the experiment. (b) Primary kaolinite. (c) EDS analysis in the No. 1 box of Figure 6(a). (d) EDS analysis in the No. 2 box of Figure 6(a). (e) EDS analysis in the box of Figure 6(b).

those of the primary kaolinite, which occurred in regular schistose arrangements (Figure 6(b)), and were thus considered to have been generated by the WCRI.

Although the fine-grained sandrock and sandy mudrock specimens exhibited similar phenomena at the fracture surfaces, the surfaces were different in terms of the types of minerals dissolved and/or corroded and the types of secondary minerals generated. As shown in Figure 7, in the fine-grained sandrock, the albite at the fracture surface also exhibited significant dissolution/corrosion, with secondary kaolinite formed on its surface, although other secondary minerals or sediments were also observed. As shown in Figure 7(d), cluster-shaped crystals were observed on the surfaces of primary minerals at the fracture, and these were confirmed to be $CaSO_4$ crystals (gypsum) based on the EDS analysis. Gypsum was not detected in the mineral composition test before the experiment (Table 1); therefore, the gypsum crystals were formed during the experiment. Based on the EDS analysis performed on the area containing gypsum crystals (Figure 7(f)), the cluster-shaped crystals also consisted of Si, Al, K, and Fe, in addition to the elements attributed to gypsum. According to the atomic ratios of these elements, potassium feldspar or plagioclases or both were mixed with the secondary gypsum crystals that fused into or developed on the surface of the primary feldspars.

Significant dissolution and/or corrosion of clay minerals were also observed at the fracture surface of the sandy mudrock specimen, in addition to the dissolution and/or corrosion of feldspars and the formation of secondary kaolinite that were also observed in the other two specimens (Figure 8). Although primary clay minerals such as illite and chlorite typically occurred as flakes before the experiment, these minerals were all fragmented after the experiment, as shown in Figure 9, indicating significant involvement of clay minerals in the WCRI. Comparing the experimental results for the three different rock types, the coarse- and fine-grained sandrocks exhibited considerably less dissolution/-corrosion of minerals at the fracture surface than the sandy mudrock specimen. This difference appeared to be related to the different mineral compositions of the three rock specimens, as discussed in further detail in Section 3.4.

3.2.2. Variations in Fracture-Surface Mineral Contents. Variations in fracture-surface mineral composition, presented in Table 1, were consistent with the microstructure variations described above. The mineral contents of the three rock specimens before and after the experiment were computed, and the results are shown in Table 3. Quartz was calculated from the potassium feldspar, and plagioclases were calculated from the clay mineral ratio, with the quartz content used as the base owing to its relatively stable chemical properties. For all three rock specimens, the contents of both the feldspars (including potassium feldspar and plagioclases) and the clay minerals decreased after the experiment. In particular, the coarse- and fine-grained sandrocks experienced a large decrease in the feldspar content but a small decrease in the clay mineral content, whereas the sandy mudrock specimen exhibited the opposite pattern. These results were consistent with the SEM results above. In addition, for all three rock specimens, the decrease in the content of fracture-surface potassium feldspar was significantly larger than that of the plagioclases, as shown in Table 3.

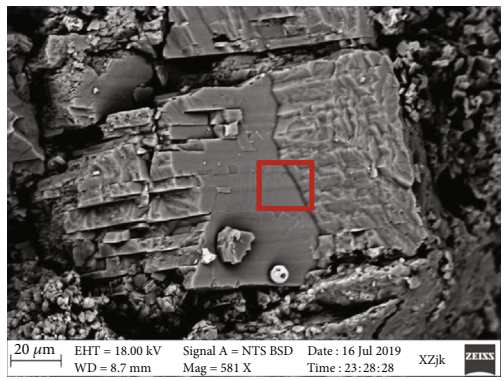

Element	Wt%	At%
O K	55.60	67.67
Na K	8.42	7.14
Al K	8.61	6.21
Si K	27.38	18.99

(a)

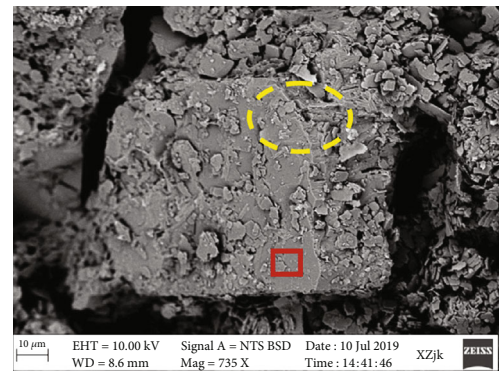

Element	Wt%	At%
O K	61.55	72.76
Na K	7.52	6.19
Al K	7.96	5.58
Si K	22.98	15.48

(b)

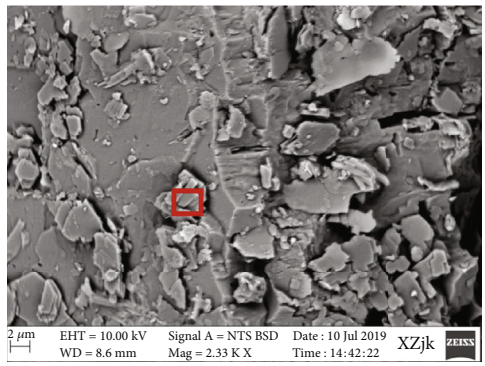

Element	Wt%	At%
O K	59.86	71.99
Al K	18.62	13.28
Si K	21.52	14.73

(c)

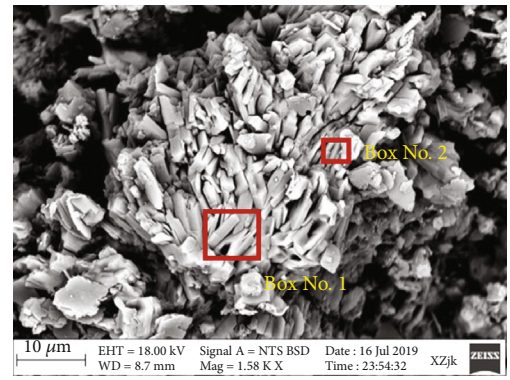

(d)

Element	Wt%	At%
O K	45.30	65.17
S K	23.74	17.04
Ca K	30.96	17.79

(e)

Element	Wt%	At%
O K	50.25	68.79
Al K	1.91	1.55
Si K	5.17	4.03
S K	18.41	12.34
K K	1.77	0.99
Ca K	22.49	12.28

(f)

Figure 7: Microstructures of fracture-surface feldspars in the fine-grained sandrock specimen before and after the experiment and secondary sediments formed on the feldspar surfaces. (a) Albite crystals (before the experiment). (b) Corroded albite crystals (after the experiment). (c) Local zoom of the ellipse marking area in (b). (d) Secondary $CaSO_4$ crystals on the fracture surface. (e) EDS analysis in the No. 1 box of (d). (f) EDS analysis in the No. 2 box of (d).

Combining the SEM and XRD results, the changes in the contents of fracture-surface minerals were attributed mainly to the dissolution and/or corrosion at the water-CO_2-rock interface. The differences between the measurements of the various specimens after the experiment were considered to result from their different mineral compositions.

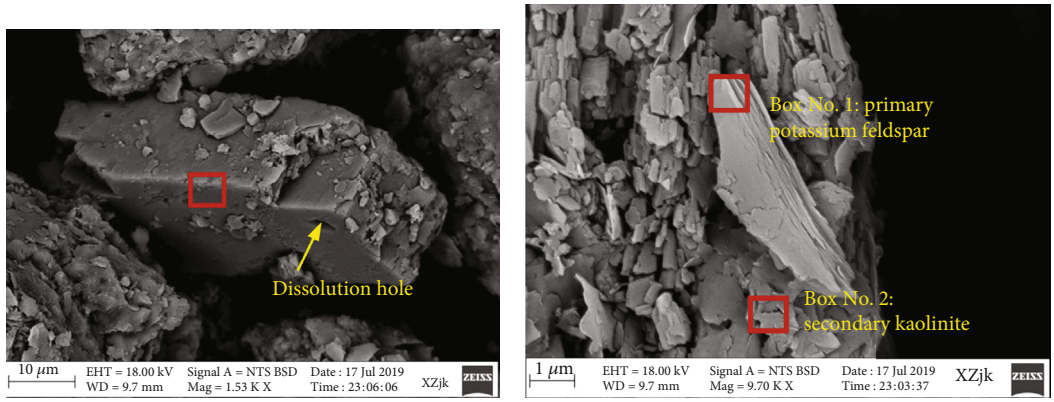

(a) (b)

Element	Wt%	At%
O K	41.38	57.81
Al K	8.98	7.43
Si K	31.50	25.07
K K	14.17	8.10
Fe K	3.96	1.59

(c)

Element	Wt%	At%
O K	41.38	57.81
Al K	8.98	7.43
Si K	31.50	25.07
K K	14.17	8.10
Fe K	3.96	1.59

(d)

Element	Wt%	At%
O K	61.91	73.98
Al K	16.89	11.96
Si K	19.94	13.58
K K	0.39	0.20
Fe K	0.88	0.30

(e)

Figure 8: Dissolution/corrosion of fracture-surface primary minerals in sandy mudrock and secondary minerals formed on the surface of the primary minerals as observed through SEM. (a) Corroded potassium feldspar crystals (dissolution hole on the crystal surface). (b) Secondary kaolinite on the surface of primary potassium feldspar. (c) EDS analysis in the box of (a). (d) EDS analysis in the No. 1 box of (b). (e) EDS analysis in the No. 2 box of (b).

3.3. Changes in the Chemical Composition of the Water Solution. Table 2 shows the ionic compositions of the water solution before and after the experiment for all three specimens. The concentrations of metal cations such as Na^+, K^+, Ca^{2+}, and Mg^{2+} increased considerably after the experiment, with the concentrations of Na^+ and Ca^{2+} increasing by large magnitudes; anions such as SO_4^{2-}, HCO_3^-, and Cl^- also increased by large magnitudes. In addition, the pH value of the water solution increased slightly, although it remained neutral. The three specimens exhibited considerable differences in terms of the magnitude of the increase in the concentration of cations and anions. The coarse- and fine-grained sandrocks exhibited markedly higher increases in the concentrations of Na^+ and SO_4^{2-} and significantly lower increases in the concentration of Mg^{2+} than the sandy mudrock specimen. The coarse-grained sandrock specimen showed a significantly lower increase in the concentration of HCO_3^- and a higher increase in the concentration of Ca^{2+} than the fine-grained sandrock and sandy mudrock specimens. The fine-grained sandrock specimen showed a higher increase in the concentration of Cl^- than the other two specimens. The different ionic concentrations were attributed to the different mineral compositions of the three rock specimens.

Based on the original mineral compositions of the three rock specimens presented in Table 1, the increase in the concentrations of metal cations such as Na^+, K^+, Ca^{2+}, and Mg^{2+} was mainly caused by the dissolution and/or corrosion of feldspars and clay minerals. In particular, the new Na^+ and Ca^{2+} cations mainly came from albite, anorthite, and a mixed illite-smectite layer; the new K^+ cations mainly came from potassium feldspar, the mixed illite-smectite layer, and illite; and the new Mg^{2+} cations mainly came from the mixed illite-smectite layer, illite, and chlorite. The sandy mudrock specimen showed the largest increase in the concentration of Mg^{2+} cations because that specimen had a markedly higher content of the mixed illite-smectite layer, illite, and chlorite (all clay minerals), compared with the other two specimens. The different increases in the concentrations of Na^+ and Ca^{2+} cations may have resulted from the different contents of albite and anorthite (both plagioclases) in the three specimens. In other words, the specimens of coarse- and fine-grained sandrocks showed larger increases in the concentrations of Na^+ and Ca^{2+} because of the higher contents of albite and anorthite in those two specimens. That the concentrations of SO_4^{2-} and Cl^- increased after the experiment may be explained by the fermentation or dissolution of some organic matters in the rock specimens.

3.4. Discussion. In the similar WCRI experiment in Ref. [22], prefractured sandy mudrock specimens were used, and groundwater was simulated using both acidic and basic water solutions. In the present experiment, two additional rock types (coarse- and fine-grained sandrocks) were simulated, and groundwater was simulated using a neutral water solution. In both experiments, the water permeability of the specimens decreased gradually. This indicates that the self-healing behavior was experimentally confirmed as occurring under different geological conditions.

3.4.1. Mechanism of Permeability Decrease. The sandy mudrock specimen exhibited staged decreases in water permeability in both the present experiment and in Ref. [22].

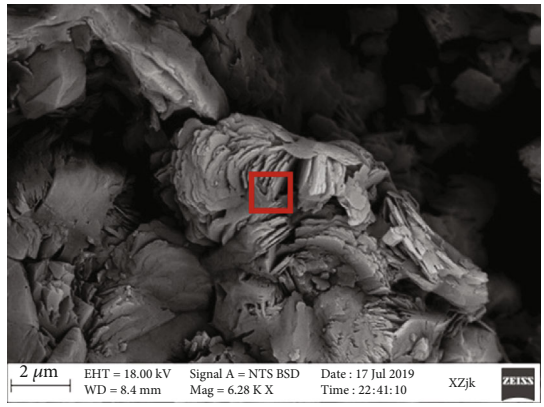

Element	Wt%	At%
O K	49.58	68.42
Mg K	2.01	1.82
Al K	11.30	9.25
Si K	14.58	11.46
K K	0.86	0.48
Fe K	21.65	8.56

(a)

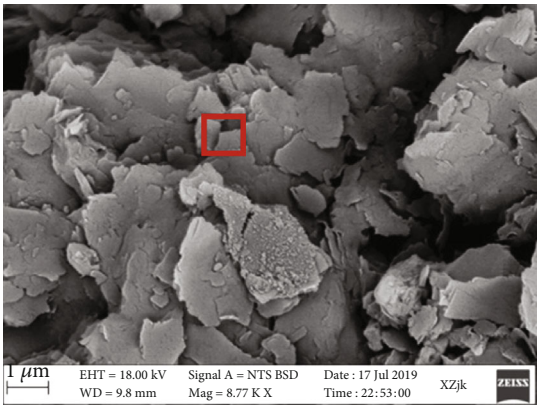

Element	Wt%	At%
O K	44.73	61.91
Mg K	2.86	2.61
Al K	13.71	11.24
Si K	21.34	16.82
K K	3.28	1.86
Fe K	14.10	5.60

(b)

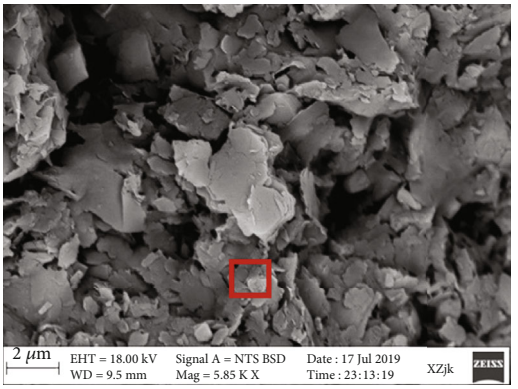

Element	Wt%	At%
O K	55.01	69.35
Mg K	0.87	0.73
Al K	11.78	8.81
Si K	24.77	17.79
K K	3.81	1.97
Fe K	3.75	1.35

(c)

Figure 9: Microstructures of fracture-surface primary clay minerals in sandy mudrock before and after the experiment. (a) Primary chlorite mineral crystals (before the experiment). (b) Corroded chlorite crystals (after the experiment). (c) Corroded illite crystals (after the experiment).

In particular, water permeability decreased rapidly during the initial stage and slowly during later stages; although in the present experiment, the initial rapidly decreasing stage was longer, and the magnitude of decrease was smaller than in the previous experiment. In the experiment in Ref. [22], the water permeability of the sandy mudrock decreased

Table 3: Fracture-surface mineral compositions of the three rock specimens before and after the experiment.

Rock samples	Before the experiment		After the experiment	
	Quartz : potassium feldspar : plagioclase : clay minerals	Potassium feldspar : plagioclase	Quartz : potassium feldspar : plagioclase : clay minerals	Potassium feldspar : plagioclase
Coarse-grained sandrock	1 : 0.55 : 0.51 : 0.06	1 : 0.92	1 : 0.46 : 0.48 : 0.06	1 : 1.04
Fine-grained sandrock	1 : 0.26 : 0.44 : 0.15	1 : 1.71	1 : 0.21 : 0.40 : 0.14	1 : 1.92
Sandy mudrock	1 : 0.44 : 0.77 : 0.26	1 : 1.76	1 : 0.32 : 0.70 : 0.25	1 : 2.21

rapidly during an initial 47-day period from 4.32×10^{-12} m^2 to 1.85×10^{-13} m^2 (by 23 times) in a basic water solution; in the acidic water solution, the initial period of 120 d exhibited a decrease from 1.06×10^{-11} m^2 to 8.71×10^{-13} m^2 (by 12 times). In the present study, the water permeability decreased rapidly during the initial 80-day period from 8.48×10^{-11} m^2 to 2.92×10^{-11} m^2 (by three times). The permeability decrease during the initial stage was mainly caused by the hydrophilic expansion of clay minerals [22]. Thus, the different water permeability decreases exhibited by the two experiments can be mainly explained by the lower total content of minerals, particularly the lower content of the mixed illite-smectite layer (which is more expansive in water), of the sandy mudrock specimen used in the present experiment.

The present experiment demonstrated that in addition to the hydrophilic expansion of clay minerals, the dissolution and/or corrosion of feldspars and other aluminum silicate minerals, which resulted in the formation of secondary minerals or crystalline sediments that filled and sealed the fractures, also contributed to the self-healing behavior of the three prefractured rock specimens. The presence of CO_2 made the feldspars and other primary aluminum silicate minerals more prone to dissolution and/or corrosion [24], a process resulting in the formation of secondary minerals through the chemical reactions represented in Eqs. (2)–(5). Furthermore, SO_4^{2-} in the Na_2SO_4 used to simulate groundwater and Ca^{2+} resulting from the dissolution and/or corrosion of anorthite can easily form sediments through a chemical reaction represented in Eq. (6). Thus, secondary kaolinite, quartz, and crystalline gypsum sediments formed through the chemical reactions induced by WCRI gradually adhered on the fracture surface of the pre-fractured rock samples, thereby sealing the fractures and decreasing their water permeability and contributing to the self-healing effect. These mechanisms can also explain the adherence of the secondary minerals adhering on minerals at the fracture surfaces, as observed through SEM (Section 3.2).

$$\text{Primary aluminum silicate minerals} + H_2O + CO_2 \leftrightarrow \text{Clay minerals} + \text{Colloids} + \text{Carbonate} + H^+ \text{or} OH^- \quad (2)$$

$$\underset{\text{Potassium feldspar}}{2K[AlSi_3O_8]} + 2H^+ + H_2O \leftrightarrow \underset{\text{Kaolinite}}{Al_2[Si_2O_5][OH]_4} + \underset{\text{Colloids}}{4SiO_2} + 2K^+ \quad (3)$$

$$\underset{\text{Albite}}{2Na[AlSi_3O_8]} + 2H^+ + H_2O \leftrightarrow \underset{\text{Kaolinite}}{Al_2[Si_2O_5][OH]_4} + \underset{\text{Colloids}}{4SiO_2} + 2Na^+ \quad (4)$$

$$\underset{\text{Anorthite}}{Ca[Al_2Si_2O_8]} + 2H^+ + H_2O \leftrightarrow \underset{\text{Kaolinite}}{Al_2[Si_2O_5][OH]_4} + Ca^{2+} \quad (5)$$

$$Ca^{2+} + SO_4^{2-} \leftrightarrow CaSO_4\downarrow \quad (6)$$

$$\underset{\text{Andesine}}{Na[AlSi_3O_8] - Ca[Al_2Si_2O_8]} + 2H^+ + K^+ \leftrightarrow \underset{\text{Sericite}}{KAl_2[AlSi_3O_{10}][OH]_2} + 2SiO_2 + Na^+ + Ca^{2+} \quad (7)$$

Due to the limitations of the experimental conditions, the WRIs were not tested under the action of loading. However, this does not affect the validity of the preceding analysis of the self-healing mechanism [21]. The experimental results further demonstrate the self-healing process. This is because, under the dissolution and/or corrosion of minerals on the fracture surface, the fracture aperture should gradually increase, and the permeability of fractured rock specimens should gradually increase as well; however, the final experimental results are contrary to this; the permeability of the rock specimens always exhibits a stable reducing trend. This indicates that self-healing reversed the adverse situation

caused by the dissolution and/or corrosion of minerals on the fracture surface.

3.4.2. Interfering Factors of the Self-Healing. The coarse- and fine-grained sandrock specimens did not exhibit the rapid permeability decrease during the initial stage found in the mudrock; although, the sandrocks did exhibit temporary rapid permeability decreases during the middle stage of the experiment. This difference can be explained by the sandrocks' lower content of the mixed illite-smectite layer and other clay minerals that exhibit greater hydrophilic expansion. The permeability decrease of these two specimens was caused by only the dissolution and/or corrosion of feldspars and other aluminum silicate minerals, as detailed in the previous paragraph. Compared with the hydrophilic expansion mechanism, this sedimentation mechanism requires a longer time to manifest and is less effective at sealing fractures.

Compared with the prefractured rock specimens used in Ref. [22], the specimens used in the present experiment had higher initial permeabilities, and the final magnitudes of the permeability decreases were smaller, even though the specimens were subjected to longer WCRIs in the present experiment. This difference was related to the fracture development morphology of the specimens and the pH value of the water solutions used. In particular, the fractures developed in the specimens in Ref. [22] were significantly less open than those used in the present experiment, and therefore, the specimens in Ref. [22] required less hydrophilic expansion of the clay minerals and smaller amounts of secondary minerals or sediments to fill and seal the fractures, enabling greater self-healing capacity in a shorter period of time. Had the present experiment been continued, the water permeability of the prefractured specimens may have continued to decrease, although probably at lower rates, because the content of the relevant components of the water solution and the amount of fracture-surface minerals would decrease gradually.

From the fracture-surface mineral compositions before and after the experiment (Table 3), the loss of potassium feldspar was markedly higher than that of plagioclases in all three specimens. However, from the ionic compositions of the water solution before and after the experiment (Table 2), the concentration of K^+ increased by the smallest magnitude. The reason for this result may have been that the precipitated K^+ was involved in the reaction represented in Eq. (7). More specifically, the dissolution and/or corrosion of potassium feldspar as represented in Eq. (3) would have generated K^+, which would then react with andesine (a type of plagioclase) and H^+ (generated by the CO_2 input into the container) to form sericite. In other words, the precipitated K^+ may have become fixed in newly generated secondary minerals and replaced Na^+ and Ca^{2+}, resulting in the markedly lower increase in the concentration of K^+ than in the concentrations of Na^+ and Ca^{2+}.

Although prefractured rock specimens with different lithological properties were capable of seal-healing in water solutions with various chemical properties under the influence of the WCRI, different secondary minerals or crystalline sediments were involved in the self-healing processes. These secondary matters had different roles in the sedimentation and sealing mechanism occurring at the fracture surface, resulting in different self-healing capacities under the various conditions. Thus, investigating the self-healing mechanisms or patterns exhibited under different physiochemical conditions in the water, air, and rock is critical to assessing the self-healing capacity of fractured rocks. The present WCRI experiment was limited in that only three rock types, all typical of the Shendong coalfield, were tested, and in that the groundwater was simulated using only a neutral water solution. Further investigation into the above problems will be conducted by changing the relevant experimental conditions, with the aim of providing insight into the mechanisms underlying the self-healing behavior of fractured rocks.

4. Conclusions

(1) A WCRI experiment on prefractured specimens of three rocks (coarse-grained sandrock, fine-grained sandrock, and sandy mudrock) typical of the Shendong coalfield was run for nearly 15 months, simulating groundwater with a neutral water solution. The water permeability of the specimens decreased gradually during the experiment, and this behavior was consistent with the field observations of self-healing of mining-damaged fractures, confirming that the phenomenon is common under different geological conditions

(2) XRD and SEM analyses elucidated the mechanism underlying the self-healing behavior of the prefractured rock specimens. In particular, the self-healing of the specimens was enabled mainly by the following two mechanisms: (1) the hydrophilic expansion of fracture-surface clay minerals to narrow fractures; and (2) the dissolution and/or corrosion of feldspars and other primary aluminum silicate minerals and the consequent ionic exchange between the primary minerals, CO_2, and water solution to generate secondary minerals or crystalline sediments that filled and sealed the fractures

(3) The fracture development morphology of the specimens and the pH value of the water solution had significant effects on the process and degree of self-healing. A smaller fracture or a fracture with a smaller initial permeability requires less hydrophilic expansion of clay minerals and a smaller amount of secondary minerals or sediments to enable the repair. Neutral and basic groundwater conditions facilitated better self-healing of fractured mudrocks rich in clay minerals, whereas acidic groundwater conditions and the presence of CO_2 facilitated better self-healing of fractured sandrocks rich in feldspars

(4) Whereas the WCRI can significantly reduce the water permeability of a fractured rock, the absolute value of its reduced water permeability remains relatively high and has yet to reach the order of magnitude of the permeability of aquicludes. This may be related to the relatively low amount of precipitates or

secondary minerals formed in relevant interactions and processes. Therefore, it remains difficult to rely solely on the self-healing behavior of fractured rocks to impart absolute impermeability to them. Based on the self-healing characteristics of different rocks in groundwaters with different chemical properties, groundwater and rocks can be engineered to alter their chemical properties and thereby facilitate rock fracture remediation and improve aquifer restoration. To decrease the permeability of fractured rocks and preserve groundwater resources, underground chemical conditions can be engineered to facilitate the formation of secondary minerals or sediments, and these derivatives can be expected to fill and seal fractures. Owing to character limitations, this paper is not intended as a thorough discussion. Other separate papers will be prepared for a more in-depth investigation

Symbols

K: Water permeability
Q: Water flow per unit time
A: Inner cross-sectional area of the container
L: Height of the rock specimen
μ: Solution's viscosity
ΔP: Pressure difference before and after water flow through the rock specimen.

Data Availability

The data used to support the finding of this study are available from the corresponding author upon request.

Conflicts of Interest

The authors declared that they have no conflicts of interest to this work.

Acknowledgments

Financial support from the Fundamental Research Funds for the Central Universities (2020ZDPYMS19) is greatly appreciated.

References

[1] J. L. Xu, *Green Mining in Coal Mines*, China University of Mining and Technology Press, Xuzhou, China, 2011.

[2] J. F. Ju, J. L. Xu, Q. S. Li, W. B. Zhu, and X. Z. Wang, "Progress of water-preserved coal mining under water in China," *Coal Science and Technology*, vol. 46, no. 1, pp. 12–19, 2018.

[3] X. Miao, X. Cui, J.'. Wang, and J. Xu, "The height of fractured water-conducting zone in undermined rock strata," *Engineering Geology*, vol. 120, no. 1-4, pp. 32–39, 2011.

[4] L. M. Fan and X. D. Ma, "A review on investigation of water-preserved coal mining in western China," *International Journal of Coal Science & Technology*, vol. 5, no. 4, pp. 411–416, 2018.

[5] Z. Zhang, R. Zhang, H. Xie, M. Gao, and J. Xie, "Mining-Induced coal permeability change under different mining layouts," *Rock Mechanics and Rock Engineering*, vol. 49, no. 9, pp. 3753–3768, 2016.

[6] L. Li, F. Li, Y. Zhang, D. Yang, and X. Liu, "Formation mechanism and height calculation of the caved zone and water-conducting fracture zone in solid backfill mining," *International Journal of Coal Science and Technology*, vol. 7, no. 1, pp. 208–215, 2020.

[7] D. Z. Gu, "Theory framework and technological system of coal mine underground reservoir," *Journal of China Coal Society*, vol. 40, no. 2, pp. 239–246, 2015.

[8] Q. S. Li, J. F. Ju, Z. G. Cao, F. Gao, and J. H. Li, "Suitability evaluation of underground reservoir technology based on the discriminant of the height of water conduction fracture zone," *Journal of China Coal Society*, vol. 42, no. 8, pp. 2116–2124, 2017.

[9] J. F. Ju, J. L. Xu, and W. B. Zhu, "Storage capacity of underground reservoir in the Chinese western water-short coalfield," *Journal of China Coal Society*, vol. 42, no. 2, pp. 381–387, 2017.

[10] H. Song, J. Xu, J. Fang, Z. Cao, L. Yang, and T. Li, "Potential for mine water disposal in coal seam goaf: investigation of storage coefficients in the Shendong mining area," *Journal of Cleaner Production*, vol. 244, article 118646, 2020.

[11] B. Amadei and W. Z. Savage, "An analytical solution for transient flow of Bingham viscoplastic materials in rock fractures," *International Journal of Rock Mechanics and Mining Sciences*, vol. 38, no. 2, pp. 285–296, 2001.

[12] R. Gothäll and H. Stille, "Fracture–fracture interaction during grouting," *Tunnelling and Underground Space Technology*, vol. 25, no. 3, pp. 199–204, 2010.

[13] A. H. Hoien and B. Nilsen, "Rock mass grouting in the Løren tunnel: case study with the main focus on the groutability and feasibility of drill parameter interpretation," *Rock Mechanics and Rock Engineering*, vol. 47, no. 3, pp. 967–983, 2014.

[14] D. Z. Gu and J. M. Zhang, "Modern coal mining affected to underground water deposit environment in west China mining area," *Coal Science and Technology*, vol. 40, no. 12, pp. 114–117, 2012.

[15] K. B. Min, J. Rutqvist, and D. Elsworth, "Chemically and mechanically mediated influences on the transport and mechanical characteristics of rock fractures," *International Journal of Rock Mechanics and Mining Sciences*, vol. 46, no. 1, pp. 80–89, 2009.

[16] J. Kaszuba, B. Yardley, and M. Andreani, "Experimental Perspectives of Mineral Dissolution and Precipitation due to Carbon Dioxide-Water-Rock Interactions," *Reviews in Mineralogy & Geochemistry*, vol. 77, no. 1, pp. 153–188, 2013.

[17] N. Kampman, M. J. Bickle, A. Maskell et al., "Drilling and sampling a natural CO2 reservoir: Implications for fluid flow and CO2-fluid–rock reactions during CO2 migration through the overburden," *Chemical Geology*, vol. 369, pp. 51–82, 2014.

[18] S. L. Felice, D. Montanari, S. Battaglia, G. Bertini, and G. Cianelli, "Fracture permeability and water–rock interaction in a shallow volcanic groundwater reservoir and the concern of its interaction with the deep geothermal reservoir of Mt. Amiata, Italy," *Journal of Volcanology and Geothermal Research*, vol. 284, pp. 95–105, 2014.

[19] J. G. Ning, X. S. Liu, Y. L. Tan, J. Wang, M. Zhang, and L. S. Zhang, "Water-preserved mining evaluation in shallow seam

with sandy mudstone roof," *Journal of Mining & Safety Engineering*, vol. 32, no. 5, pp. 814–820, 2015.

[20] O. T. Mendoza, J. Ruiz, E. D. Villasenor et al., "Water-rock-tailings interactions and sources of sulfur and metals in the subtropical mining region of Taxco, Guerrero (southern Mexico): a multi-isotopic approach," *Applied Geochemistry*, vol. 66, no. 3, pp. 73–81, 2016.

[21] J. Ju, Q. Li, J. Xu, X. Wang, and J. Lou, "Self-healing effect of water-conducting fractures due to water-rock interactions in undermined rock strata and its mechanisms," *Bulletin of Engineering Geology and the Environment*, vol. 79, no. 1, pp. 287–297, 2020.

[22] J. F. Ju, Q. S. Li, J. L. Xu, and L. Yang, "Water-CO_2-rock interaction experiments to reveal the self-healing effect of fractured mining damaged rock," *Journal of China Coal Society*, vol. 44, no. 12, pp. 3701–3710, 2019.

[23] C. Li, J. Qi, S. Wang et al., "A holistic system approach to understanding underground water dynamics in the loess tableland: a case study of the Dongzhi loess tableland in northwest China," *Water Resources Management*, vol. 28, no. 10, pp. 2937–2951, 2014.

[24] L. P. Qiao, J. Liu, and X. T. Feng, "Study on damage mechanism of sandstone under hydro-physico-chemical effects," *Chinese Journal of Rock Mechanics and Engineering*, vol. 26, no. 10, pp. 2117–2124, 2007.